10.1 MISOVORTICES WITHIN THE 07 JANUARY 2014 LONG LAKE-AXIS-PARALLEL LAKE-EFFECT SNOW BAND DURING THE ONTARIO WINTER LAKE-EFFECT SYSTEMS PROJECT

Jake P. Mulholland*, Jeffrey W. Frame
University of Illinois at Urbana-Champaign, Urbana, Illinois

Scott M. Steiger
State University of New York at Oswego, Oswego, New York

1. INTRODUCTION

The winter of 2013-2014 featured an extensive field campaign to examine lake-effect snow storms called the Ontario Winter Lake-effect Systems (OWLeS) Project (Kristovich et al. 2016). The three main objectives of the project were: 1) to examine the kinematics and dynamics of long lake-axis-parallel (LLAP; Steiger et al. 2013) snow bands, 2) upwind and downwind lake influences (i.e., heat and moisture fluxes and subsequent advection) on lake-effect convection, and 3) orographic influences on lake-effect convection. The platforms that were utilized during the project included: Three X-band Doppler-on-Wheels (DOW) radars (provided by the Center for Severe Weather Research), five (four mobile) rawinsonde systems, the University of Wyoming King Air (UWKA) aircraft, and the University of Alabama in Huntsville's Mobile Integrated Profiling System (MIPS).

Previous lake-effect snow research has primarily focused on the western Great Lakes, such as Lake Michigan and Lake Superior. Studies such as Forbes and Merritt (1984) and Laird et al. (2001) documented instances of mesovortices (diameters [D] > 4000 m; Fujita 1981) forming over the lakes during instances of weak background synoptic flow (e.g., Niziol et al. 1995, Type-V bands). The mesovortices typically appeared to either exhibit a braided structure or occur as a single vortex with an eye-like feature. These mesovortices were typically accompanied by weak cyclonic low-level rotation, brief bursts of heavier snow, and gusty winds (Forbes and Merritt 1984).

A more recent field campaign, the Long Lake-Axis-Parallel (LLAP) Project, occurred during the winter of 2010-2011 over Lake Ontario and surrounding downwind (i.e., south and east) locations. The main goal of this project was to obtain fine-scale Doppler radar observations of LLAP bands, which had never been attempted before.

The project recorded observations of mesovortices (D > 4000 m), misovortices (also known as misocyclones; Fig. 1; D ~ 40-4000 m), horizontal vortices, horizontal shear zones (Fig. 1), bounded weak echo regions, outflow boundaries, and anvils within the LLAP bands (Steiger et al. 2013). The mesoscale vortices sometimes altered the morphology and orientation of the bands, which has implications for weather forecasters attempting to predict snowfall intensity, amount, and location. Hence, this research is aimed to understand the underlying dynamics of these miso- and mesovortices and the processes that aid in their development, maintenance, and ultimate demise. One event from the OWLeS project in which an abundance of misovortices occurred was on 07 January 2014. This case is the focus for this research.

2. OVERVIEW OF THE 07 JANUARY 2014 LAKE-EFFECT EVENT

Throughout the winter of 2013-2014, frequent intrusions of Arctic air masses occurred over most of the eastern 2/3^{rds} of the Contiguous United States. 07 January 2014 was just one such case from this anomalously cold winter. The 0000 UTC/07 Jan 2014 Rapid Refresh (RAP) model 500-hPa analysis reveals a highly-amplified pattern with a deep trough over the eastern U.S. and a ridge over the western U.S. (Fig. 2). A shortwave trough was located west of Lake Ontario, over Lower Michigan (Fig. 2). This shortwave trough traversed Lake Ontario between 0400-0800 UTC. Quasi-geostrophic forcing for ascent ahead of the approaching

---

* *Corresponding author address*: Jake P. Mulholland, University of Illinois at Urbana-Champaign, Dept. of Atmospheric Sciences, Urbana, IL, 61801; email: jmulhol2@illinois.edu

shortwave trough overspread the region, forcing the capping inversion atop the Arctic air mass over Lake Ontario to rise. A sounding launched from Henderson Harbor, NY, at 0816 UTC revealed a moist and conditionally unstable boundary layer extending vertically to around 540 hPa (Fig. 3). With 850-hPa temperatures around -25˚C above a lake with a surface water temperature around 3˚C, thermodynamic conditions were more than adequate to support the development of an intense LLAP band (Fig. 4).

One aspect of this case that is of particular interest for this research was the presence of misovortices along a wind shift within the LLAP band. Figure 5 displays a string of misovortices at 0524 UTC, with diameters (defined here as distance between local max/min values of radial velocity derived from single-Doppler observations) ranging from 1-3 km and approximate regular spacing around 5 km. The misovortices were located along the northern edge of the band, corresponding to a sharp N-S horizontal gradient in reflectivity (Fig. 5a). Also, a cyclonic horizontal shear zone was present along which the misovortices were propagating, as seen by the faster inbound velocities (darker green colors) to the south of the misovortices and the slower inbound velocities (lighter green colors) seen to the north of the misovortices (Fig. 5b).

Figure. 6 at 0744 UTC, reveals that the western end of the string of misovortices was propagating from west-to-east across Lake Ontario. The shear zone was now closer to the center of the band, with the edges of the band appearing more diffuse in the reflectivity field. Further inspection of the background synoptic regime reveals that an upstream connection with another LLAP band over Georgian Bay was present from 0400-0700 UTC (Fig. 7). This upstream connection ceased around 0700 UTC as boundary-layer winds backed from northwesterly to westerly over Georgian Bay following the passage of the aforementioned 500-hPa shortwave trough and the approach of a midlevel ridge from the west (Fig. 8). The downstream advection of heat and moisture from upstream lakes affecting downwind lake-effect storms has been documented in the literature (e.g., Rodriguez et al. 2007). However, the development of misovortices in this case appears to display a dependence on Georgian Bay or possibly Lake Superior. Once the upstream connection ceased, the string of misovortices disappeared and instances of only isolated vortices prevailed throughout the remainder of the event.

A 1 km Weather Research and Forecasting [WRF; initialized with Rapid Refresh (RAP) model at 0300 UTC/07 January 2014] model valid at 0700 UTC illustrates the string of vortices extending southeastward from Georgian Bay, where the vortices appear to originate, toward the eastern portions of Lake Ontario (Fig. 9). This simulation is consistent with observations from the King City, Ontario, radar that depicts misovortices moving downwind from Georgian Bay toward Lake Ontario. It is worth noting that WSR-88D radar data within the band over the northwestern portions of Lake Ontario from Montague, NY (KTYX), and Buffalo, NY (KBUF), is sparse owing to the relatively shallow nature of the band (between 2-3 km deep) in comparison to the radar beam height in that area (i.e., the KBUF 0.5˚ beam height was approximately 2 km above ground level [AGL] at a distance of 120 km from the radar over NW Lake Ontario). This precludes any low-level (< 1 km AGL) radar observations of vortices or most other features of interest within the band in this region.

3. METHODOLOGY

Further inspection of the misovortices was made possible with the use of dual-Doppler (DD) analyses. Figure 10 displays the asset map with the approximate DD lobe from DOW6 and DOW8 drawn in red. Using a two-pass Barnes analysis, data from these radars were mapped to a 40 x 40 x 2.5 km grid with a horizontal and vertical grid spacing of 250 m. The horizontal smoothing parameter chosen was 0.747 km^2 and the vertical smoothing parameter was 0.400 km^2 based upon $\kappa = (1.33\delta)^2$ (Pauley and Wu 1990; Marquis et al. 2007).

4. DUAL-DOPPLER ANALYSES OF THE MISOVORTICES

Figures 11a-d displays a DD wind synthesis at 0524 UTC. A confluence zone is evident in Fig. 11a near the northern edge of the band along the 20 dBZ reflectivity contour. The confluence line is also aligned with the region of maximum updrafts at 500 m AGL (Figs. 11b, c). Maximum updraft speeds at this level are between 1.5 – 2.5 m s^{-1} (Fig. 11c). Most vortices are observed to weaken significantly above 1 km AGL, presumably owing to the dearth of band-induced low-level stretching amplification above this level. Hence, these analyses were performed at 500 m AGL.

The reflectivity appendages seen in Fig. 11a correspond to patches of enhanced positive vertical vorticity (roughly circular regions of purple shading) at 500 m AGL in Fig. 11d and likely arise from the advection of hydrometeors around the northern sides of the circulations. The maximum value of vertical vorticity within the vortices is approximately 3.0 x 10^{-2} s^{-1}. These values are within the range of those found by other studies that focused on misovortices, albeit in lower latitudes over land and during the spring months. DD results from the International H_2O Project (IHOP_2002; Weckwerth et al. 2004), which examined misovortices along low-level convergence zones over the Southern Great Plains, exhibited maximum vertical vorticity values on the order of ~1.3 x 10^{-2} s^{-1} (Marquis et al. 2007). Mueller and Carbone (1987) observed misovortices developing along a thunderstorm outflow boundary on 19 June 1984; their results show that maximum values of vertical vorticity were on the order of ~5.3 x 10^{-2} s^{-1} in that case.

Not surprisingly, this string of misovortices is along a horizontal wind shift near the northern edge of the band. Fig 11b illustrates that higher values of the zonal wind component (~20 m s^{-1}) to the south of the confluence line (warm colors) while lower values of the zonal wind component (~5 m s^{-1}) are seen to the north of the confluence line (cool colors). This suggests that the misovortices were likely forming from horizontal shear instability (HSI). More on this hypothesis is found in section 5 below.

Figures 12a-d displays a DD wind synthesis at 0744 UTC. The confluence zone has shifted southward toward the center of the band and is more subtle (Fig. 12a). The reflectivity structure associated with the band was also more symmetric at this time, whereas at 0524 UTC, the band was asymmetric with a sharp horizontal reflectivity gradient along the northern edge and a diffuse southern edge. The area covered by reflectivity values greater than 20 dBZ was also smaller by this time. Updraft speeds also decreased, with maximum values of ~2.5 m s^{-1} at 0524 UTC compared to ~2.0 m s^{-1} at 0744 UTC (Fig. 12c). The ribbon of maximum updraft speeds was slightly north of the center of the band at this time.

Figure 12d depicts the lack of vortices at 0744 UTC, in stark contrast to what was seen at 0524 UTC (Fig. 11). This transition is coincident with the passage of the 500-hPa shortwave trough and approach of the midlevel ridge which lead to the termination of the upstream connection with Georgian Bay (as discussed above). The maximum vertical vorticity values decrease along the shear zone by 0744 UTC (Fig. 12d) and are only on the order of ~0.8 x 10^{-2} s^{-1} (as compared to ~3.0 x 10^{-2} s^{-1} at 0524 UTC). Additionally, the decrease in the band-induced mesoscale updraft strength likely restricted subsequent amplification via low-level vortex stretching. After this time, only isolated instances of misovortices were observed.

5. HORIZONTAL SHEAR INSTABILITY

The development of strings of misovortices has been attributed to the release of horizontal shear instabilities based upon both observational and modeling studies (e.g., Mueller and Carbone 1987; Lee and Wilhelmson 1997; Marquis et al. 2007). Boundaries featuring large horizontal wind shear (i.e., drylines, cold fronts, outflow boundaries) are favored regions for misovortexgenesis. In an attempt to support the hypothesis that HSI is the main driver for the development of the misovortices observed on 07 January 2014, two HSI conditions were analyzed. The first condition, Rayleigh's Stability Criterion, states that $\boldsymbol{\beta} - \frac{\partial^2 \bar{u}}{\partial^2 y}$, where $\boldsymbol{\beta}$ **= df/dy** and $\bar{\boldsymbol{u}}$ is the zonally averaged zonal wind, must change sign somewhere within the flow (see Markowski and Richardson 2010, pg. 63-64, for a full derivation). However, since $\boldsymbol{\beta}$ is of order ~10^{-11} m^{-1} s^{-1} on the mesoscale, it can be ignored, leaving the change of sign of the second term, $\frac{\partial^2 \bar{u}}{\partial^2 y}$, as the instability criterion. This is a necessary, yet insufficient condition for instability, however. In other words, there must be an inflection point within the $\bar{\boldsymbol{u}}$ profile. A more stringent condition developed by Fjørtoft (1950) states that $\frac{\partial^2 \bar{u}}{\partial^2 y}(\bar{\boldsymbol{u}} - \bar{\boldsymbol{u}}_{\boldsymbol{I}}) < \mathbf{0},$ where $\bar{\boldsymbol{u}}_{\boldsymbol{I}}$ is the base state zonal wind at the inflection point (found from Rayleigh's Stability Criterion above; i.e., $\bar{\boldsymbol{u}}_{\boldsymbol{I}}$ = 21 m s^{-1} at 0630 UTC, Fig. 14 below) must be satisfied somewhere within the flow. This again is a necessary, yet insufficient condition for instability.

Figures 13a-d is a DD analysis at 0630 UTC. Similar to 0524 UTC, a distinct cyclonic shear zone is found along the northern half of the band along which a string of misovortices exists (Fig. 13b and d). Figure 14a depicts the $\bar{\boldsymbol{u}}$

profile (as a function of *y*), averaged over every *x*-value, with an inflection point seen around *y* = 13 km (corresponding to the location of the shear zone and the vortices in Fig. 13b; also a sign change of $\frac{\partial^2 \bar{u}}{\partial^2 y}$ in Fig. 14b). Hence, both plots (Figs. 14a, b) support the hypothesis that HSI was the likely cause of the development of the misovortices. There are other locations that meet Rayleigh's Stability Criterion; however, these data are dominated by small-scale noise. A smoother is planned to be used on these data to lessen the influence of the background noise.

Fjørtoft's Stability Criterion $[\frac{\partial^2 \bar{u}}{\partial^2 y}(\bar{\boldsymbol{u}} - \bar{\boldsymbol{u}}_I) < \boldsymbol{0}]$ is plotted in Fig. 15. Outside of the noise, the main area of interest where large negative values exist is around *y* = 15 km. Hence, this more stringent criterion for instability is also met in the same region where vortices are present (Figs. 13b, d). More DD-analyses performed at a variety of times are necessary to ascertain a level of robustness for these stability criterions.

6. DISCUSSION & CONCLUSIONS

07 January 2014 featured a long-duration (> 20 h) LLAP band that affected regions downwind of Lake Ontario. This event also exhibited numerous instances of misovortices. A string of misovortices occurred between 0400-0800 UTC, followed by a regime consisting of only isolated misovortices. The main hypothesis for the development of the misovortices is the release of horizontal shear instability (HSI). This has been previously hypothesized by Steiger et al. (2013) for explaining the observation of misovortices within LLAP bands. A conceptual model from Marquis et al. (2007) summarizes an ideal situation for misocyclogenesis during IHOP (see Fig. 14 from Marquis et al. 2007). Since both Rayleigh's and Fjørtoft's Stability Criterions are met, our analyses strongly support the hypothesis that HSI is the main mechanism for the development of these misovortices. Once fully developed, it is likely that the band-induced mesoscale updraft further amplifies or maintains the misovortices through low-level vortex stretching processes. However, more work needs to be conducted to analyze vortex interactions/mergers along with vortex spacing.

Additionally, Georgian Bay and/or Lake Superior appeared vital to the development of the string of misovortices in this case because once the upstream connection ceased, the string of misovortices over Lake Ontario vanished. One hypothesis is that the geometry of Georgian Bay (Figs. 7-9), which forms a v-shape at its southeast end, favors a funneling effect of the low-level wind field, perhaps locally increasing convergence and favoring the spin-up of misovortices. However, more research into this hypothesis is needed and is currently being conducted.

A final unanswered question is more general: Why does the horizontal shear zone (along which the misovortices develop) form in the first place? This is the key question behind the misovortices associated with these LLAP bands. Could it be a result of the secondary circulation (i.e., in-up-out) within the LLAP band that helps focus low-level convergence beneath the mesoscale updraft or is it more complicated? For example, do the shear zones form owing to an enhanced pressure gradient on the southern side of the LLAP bands, locally increasing the westerly high momentum air in this particular region of the band (see Steiger et al. 2013 discussion section for additional insight)? These are questions left for further inspection and future research. The continual push to understand the underlying mechanisms that govern the formation, maintenance, and demise of these convergence and shear zones, associated misovortices, and upstream connections will likely be particularly useful to operational forecasters concerned with snowfall amount, location, and intensity from these often intense LLAP bands.

7. ACKNOWLEDGMENTS

The authors would like to thank the many participants of the OWLeS Project who collected data in often formidable and adverse weather conditions. We are also grateful to: Rachel Humphries and Paul Robinson of CSWR who helped tremendously in the post-processing of the DOW data; Drs. Karen Kosiba and Joshua Wurman of CSWR for their insight into misovortices and their development and maintenance; Dr. Robert Ballentine, Dillon Ulrich, and Andrew Janiszeski of SUNY Oswego for assistance with the WRF simulation, Christopher Johnston of the University of Illinois at Urbana-Champaign for creating the asset map; Ben Vega-Westhoff and David Wojtowicz of the University of Illinois at Urbana-Champaign for computing assistance; and Janice Mulholland for her useful comments on this paper. Support for this work was made possible by NSF Grant AGS 12-59257.

8. REFERENCES

Barnes, S. L., 1964: A technique for maximizing details in numerical weather map analysis. *J. Appl. Meteor.*, **3**, 396–409.

Forbes, G. S. and J. H. Merritt, 1984: Mesoscale vortices over the Great Lakes in wintertime. *Mon. Wea. Rev.*, **112**, 377–381.

Fujita, T. T., 1981: Tornadoes and downbursts in the context of generalized planetary scales. *J. Atmos. Sci.*, **38**, 1511–1534.

Holroyd, E. W., III, 1971: Lake-Effect Cloud Bands as Seen From Weather Satellites. *J. Atmos. Sci.*, **28**, 1165–1170.

Kristovich and Coauthors, 2000: The lake-induced convection experiment and the snow band dynamics project. *Bull. Amer. Meteor. Soc.*, **81**, 519–542.

Laird, N. F., L. J. Miller, and D. A. R. Kristovich, 2001: Synthetic dual-Doppler analysis of a winter mesoscale vortex. *Mon. Wea. Rev.*, **129**, 312–331.

Lee, B. D. and R. B. Wilhelmson, 1997: The numerical simulation of non-supercell tornadogenesis. Part I: Initiation and evolution of pretornadic misocyclone circulations along a dry outflow boundary. *J. Atmos. Sci.*, **54**, 32–60.

Markowski, P. and Y. Richardson, 2010: *Mesoscale Meteorology in the Midlatitudes*. Wiley-Blackwell, 407 pp.

Marquis, J. N., Y. P. Richardson, and J. M. Wurman, 2007: Kinematic observations of misocyclones along boundaries during IHOP. *Mon. Wea. Rev.*, **135**, 1749–1768.

Miles, J. W. and L. N. Howard, 1964: Note on a heterogeneous shear flow. *J. Fluid Mech.,* **20,** 331–336.

Mueller, C. K. and R. E. Carbone, 1987: Dynamics of a thunderstorm outflow. *J. Atmos. Sci.,* **44,** 1879–1898.

Niziol, T. A., W. R. Snyder, and J. S. Waldstreicher, 1995: Winter weather forecasting throughout the eastern United States. Part IV: Lake effect snow. *Wea. Forecasting*, **10**, 61–77.

Pauley, P. M. and X. Wu, 1990: The theoretical, discrete, and actual response of the Barnes objective analysis scheme for one and two-dimensional fields. *Mon. Wea. Rev.*, **118**, 1145–1163.

Reinking, R. F., and Coauthors, 1993: The Lake Ontario Winter Storms (LOWS) project. *Bull. Amer. Meteor. Soc.*, **74**, 1828–1849.

Rodriguez, Y., D. A. R. Kristovich, and M. R. Hjelmfelt, 2007: Lake-to-lake cloud bands: Frequencies and locations. *Mon. Wea. Rev.*, **135**, 4202–4213.

Steiger, S. M. and Coauthors, 2013: Circulations, bounded weak echo regions, and horizontal vortices observed within long-lake-axis-parallel–lake-effect storms by the Doppler on Wheels. *Mon. Wea. Rev.*, **141**, 2821–2840.

Weckwerth, T. M., and Coauthors, 2004: An overview of the International H2O Project (IHOP_2002) and some preliminary highlights. *Bull. Amer. Meteor. Soc.*, **85**, 253–277.

9. FIGURES

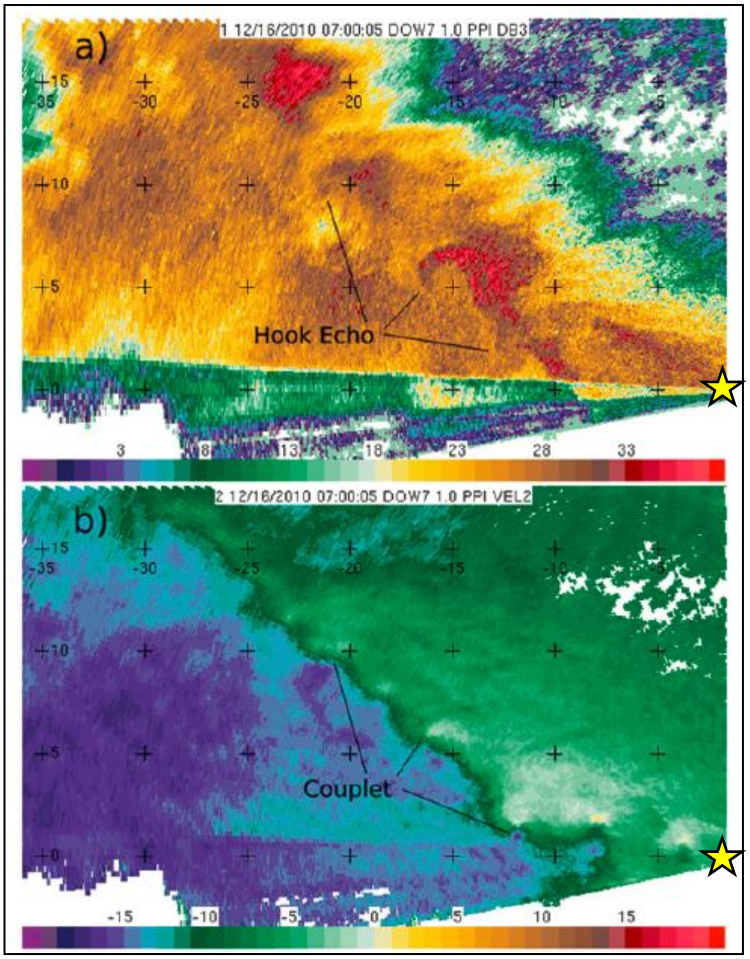

Figure 1. DOW7 observations of a) radar reflectivity (dBZ) and b) Doppler radial velocity (m s^{-1}) at 07:00:05 UTC 16 December 2010. Note how the hook echoes in the reflectivity field correspond to the couplets in the velocity field. The yellow star denotes the location of DOW7 (Figure courtesy: Steiger et al. 2013).

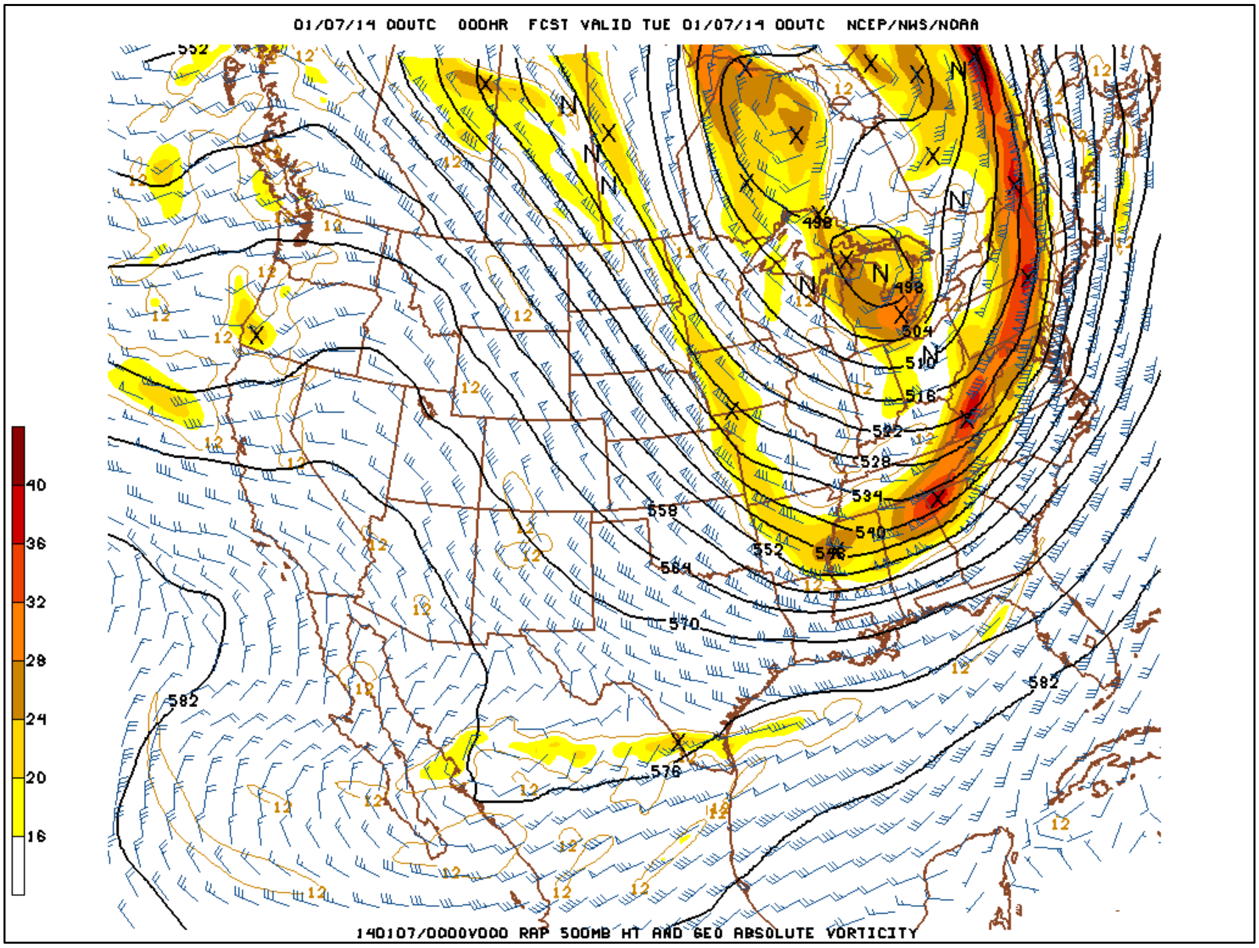

Figure 2. Rapid Refresh (RAP) model 500-hPa analysis valid at 0000 UTC 07 January 2014. Geopotential height (Dm) is in solid black contours, wind barbs (kts) are in blue, and geostrophic absolute vorticity is shaded every 4 x 10^{-5} s^{-1} starting at 16 x 10^{-5} s^{-1} (Figure courtesy: OWLeS Field Catalog - http://catalog.eol.ucar.edu/owles).

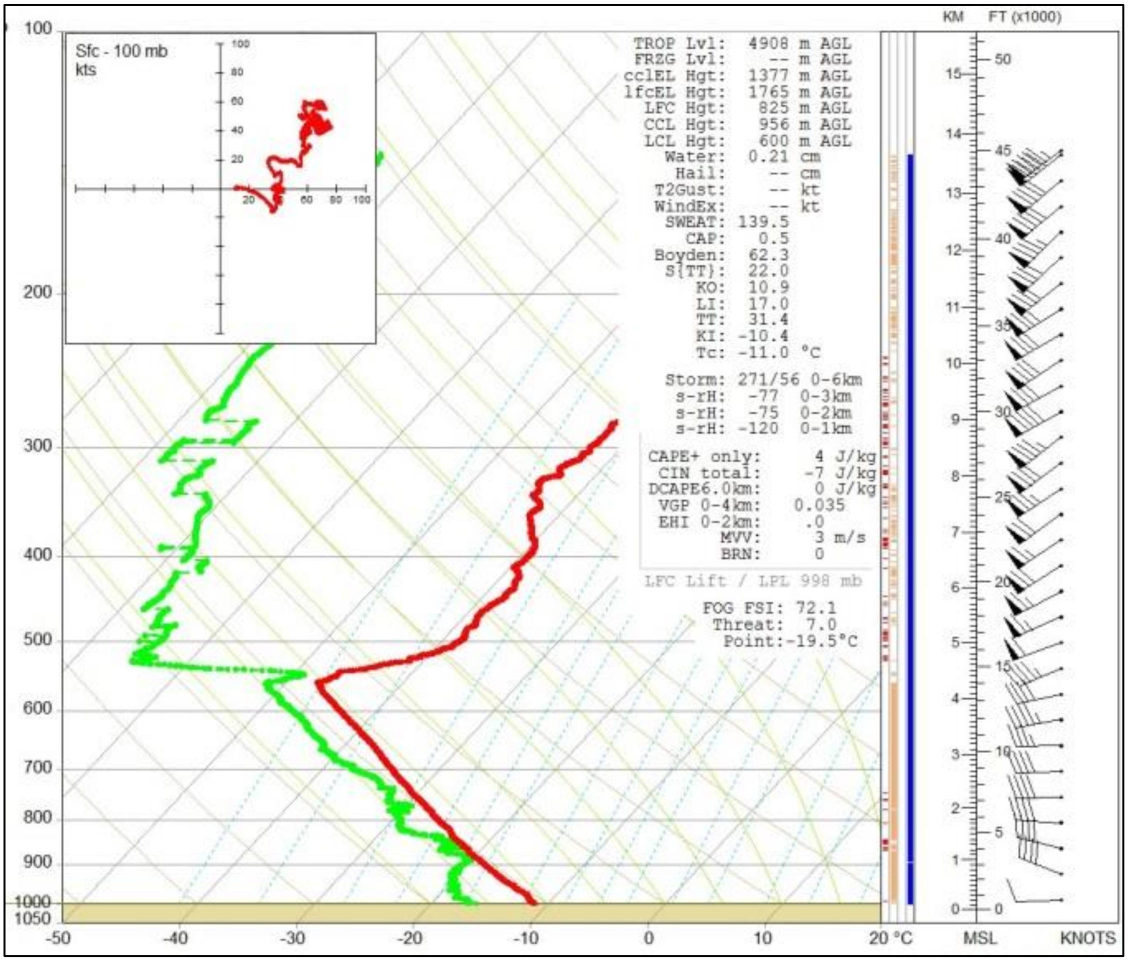

Figure 3. Sounding launched at 0816 UTC 07 January 2014 from Henderson Harbor, NY (denoted by the red star in Fig. 4). The red line indicates temperature (˚C) and the green line indicates dewpoint temperature (˚C). Winds (kts) are plotted along the right side of the image using standard meteorological notation.

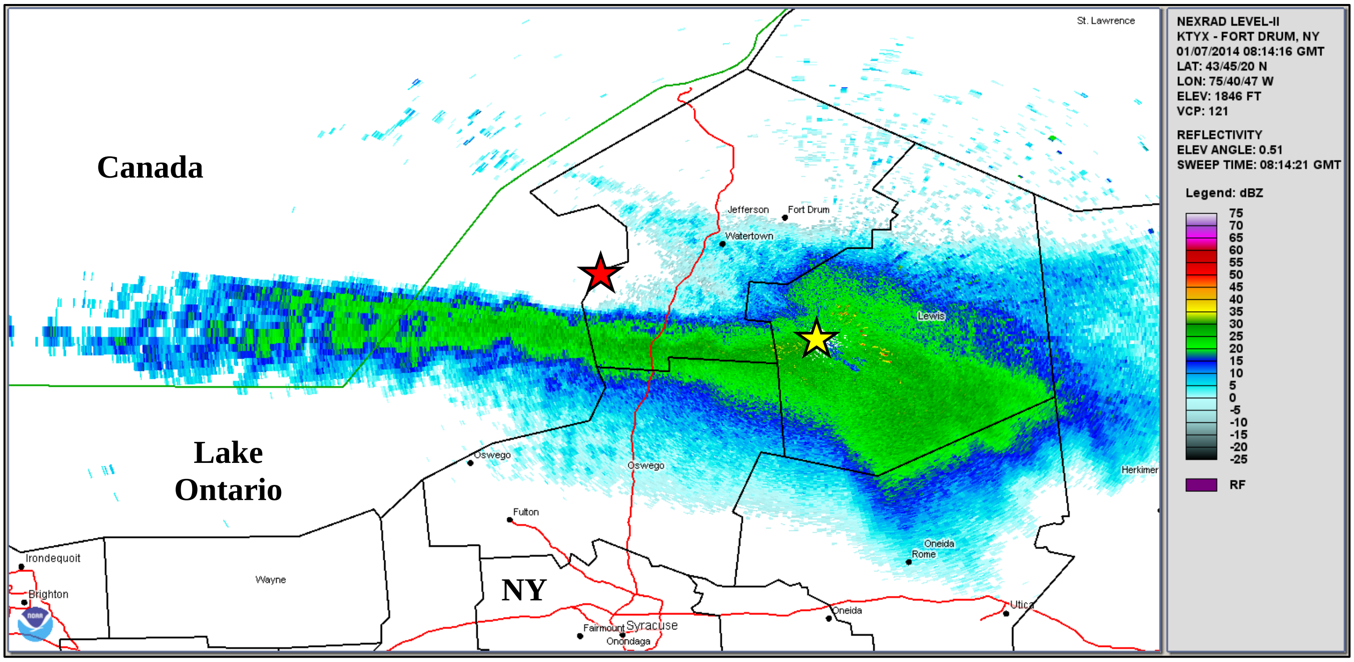

Figure 4. Radar reflectivity at 0.5˚ from Montague, NY (KTYX), at 08:14:16 UTC 07 January 2014. The yellow star indicates the location of KTYX. The red star indicates the location of the sounding launched at 0816 UTC at Henderson Harbor, NY (see Fig. 3; Figure created using the NOAA Weather and Climate Toolkit).

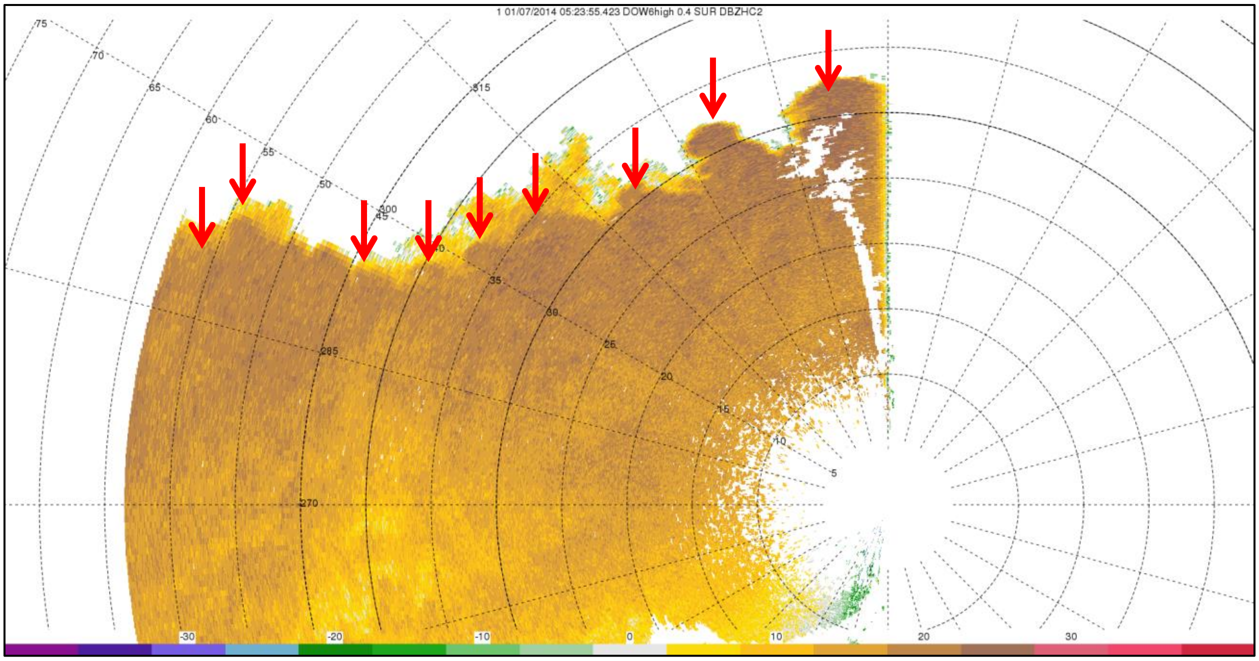

Figure 5a. 0.4˚ DOW6 reflectivity (dBZ) at 05:23:55 UTC 07 January 2014. Range rings are plotted every 5 km and azimuth angles are plotted every 15˚. Each individual vortex center is annotated with a red arrow.

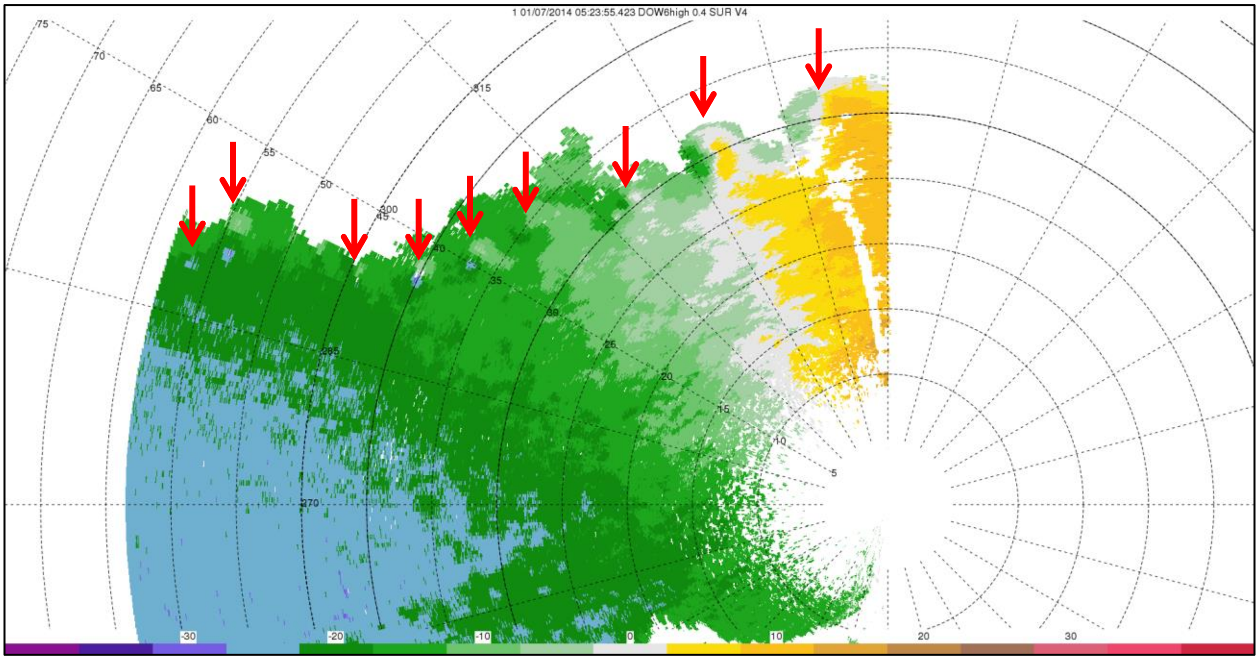

Figure 5b. As in Fig. 5a, but radial velocity (m s^{-1}).

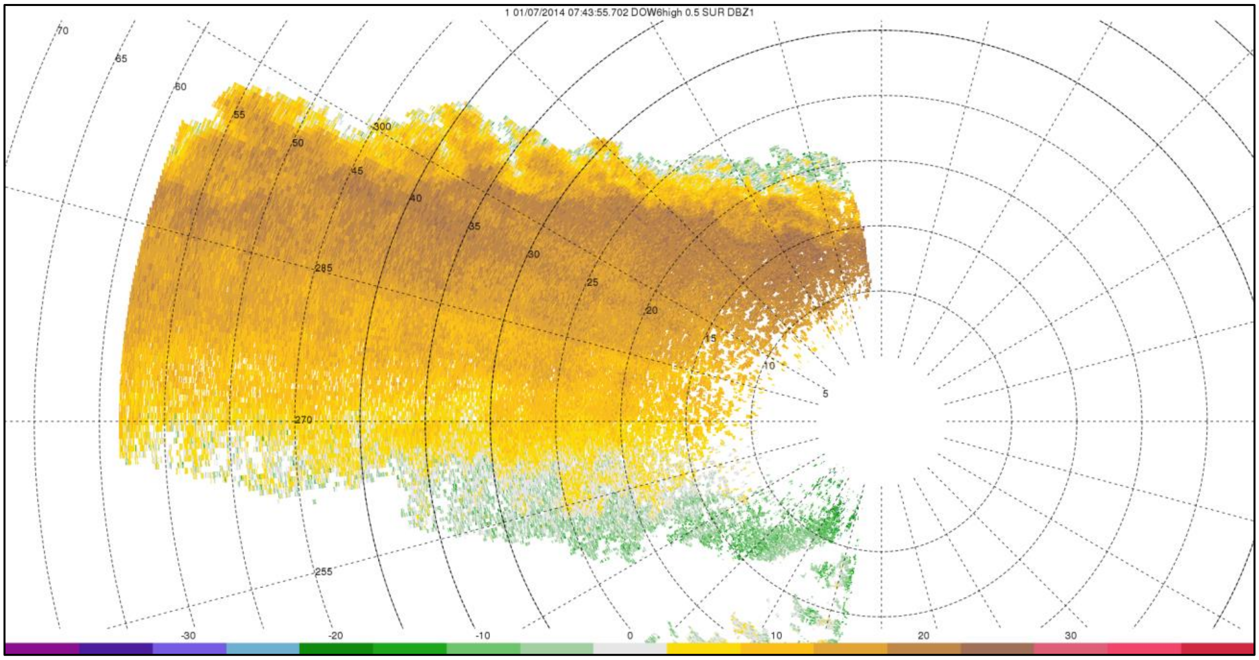

Figure 6a. As in Fig. 5a, but at 07:43:55 UTC.

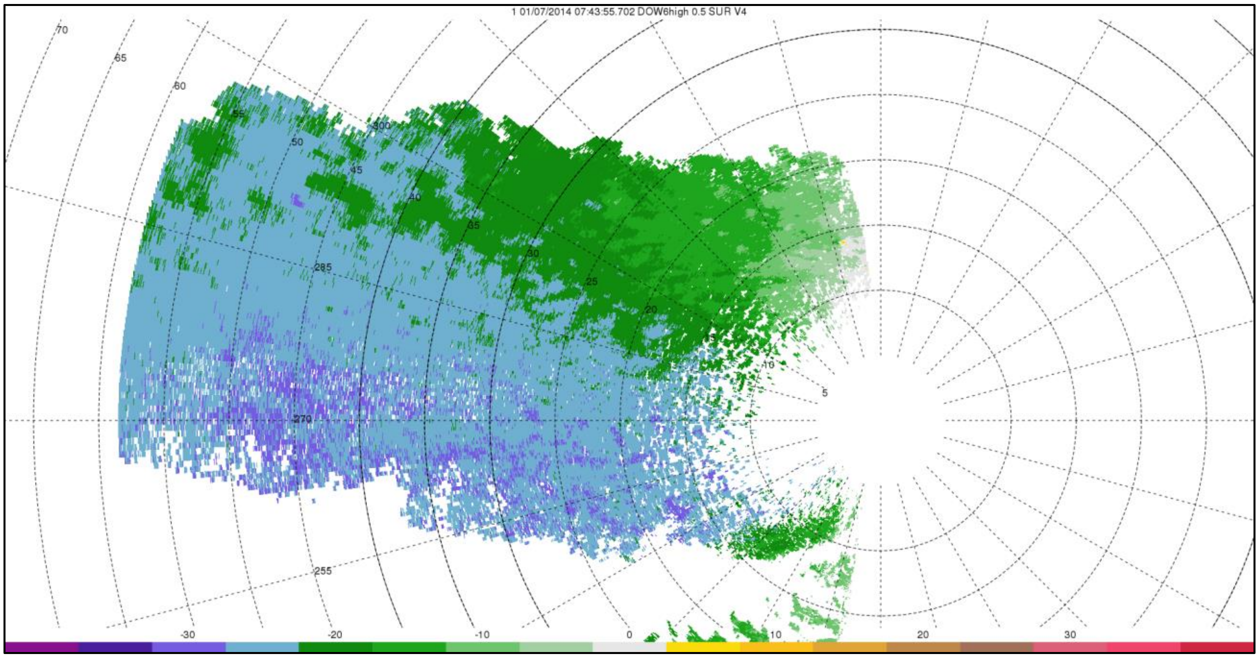

Figure 6b. As in Fig. 5b, but at 07:43:55 UTC.

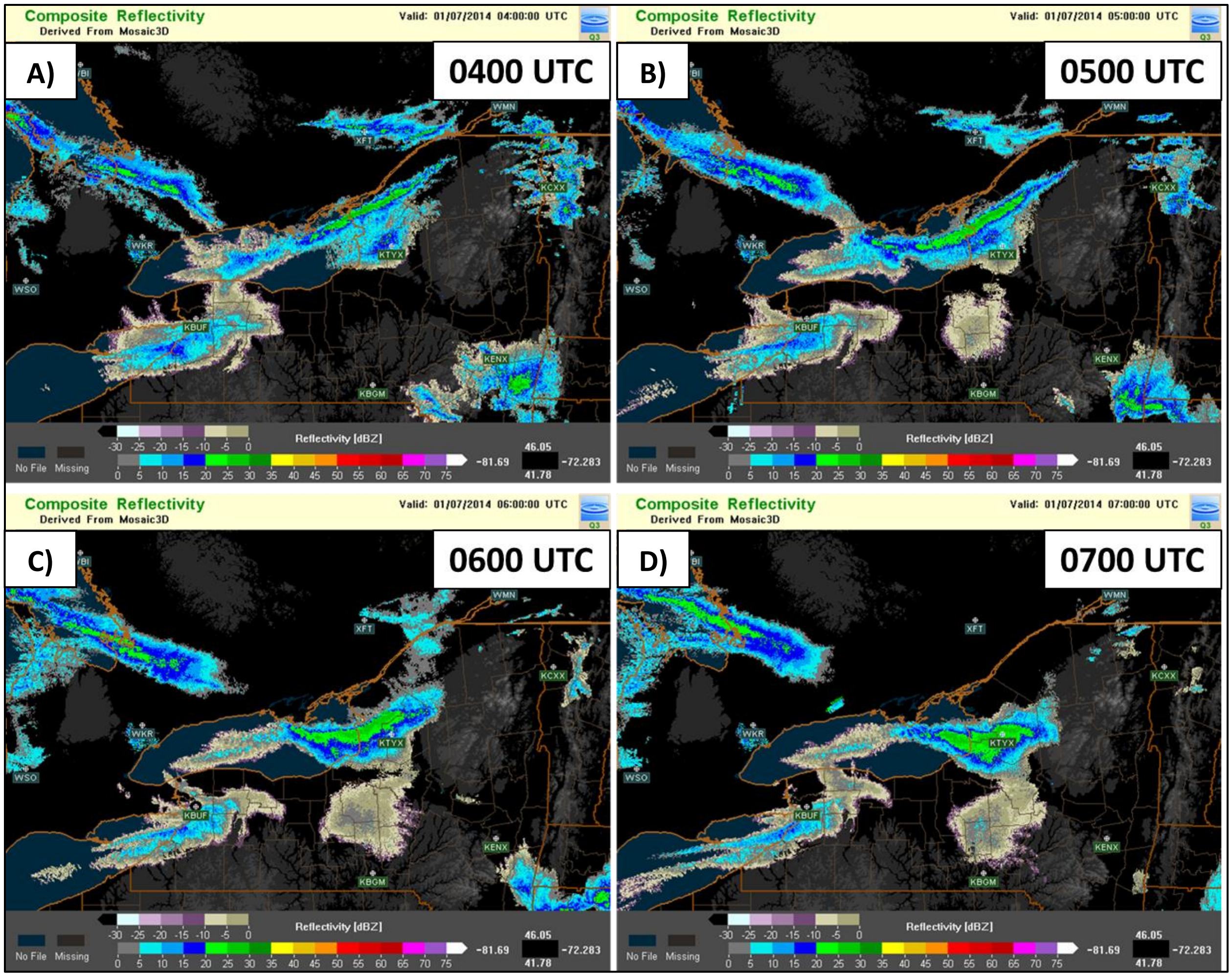

Figure 7. Multi-Radar Multi-Sensor (MRMS) System composite reflectivity (dBZ) and terrain (grayscale background) valid at: a) 0400 UTC, b) 0500 UTC, c) 0600 UTC, and d) 0700 UTC.

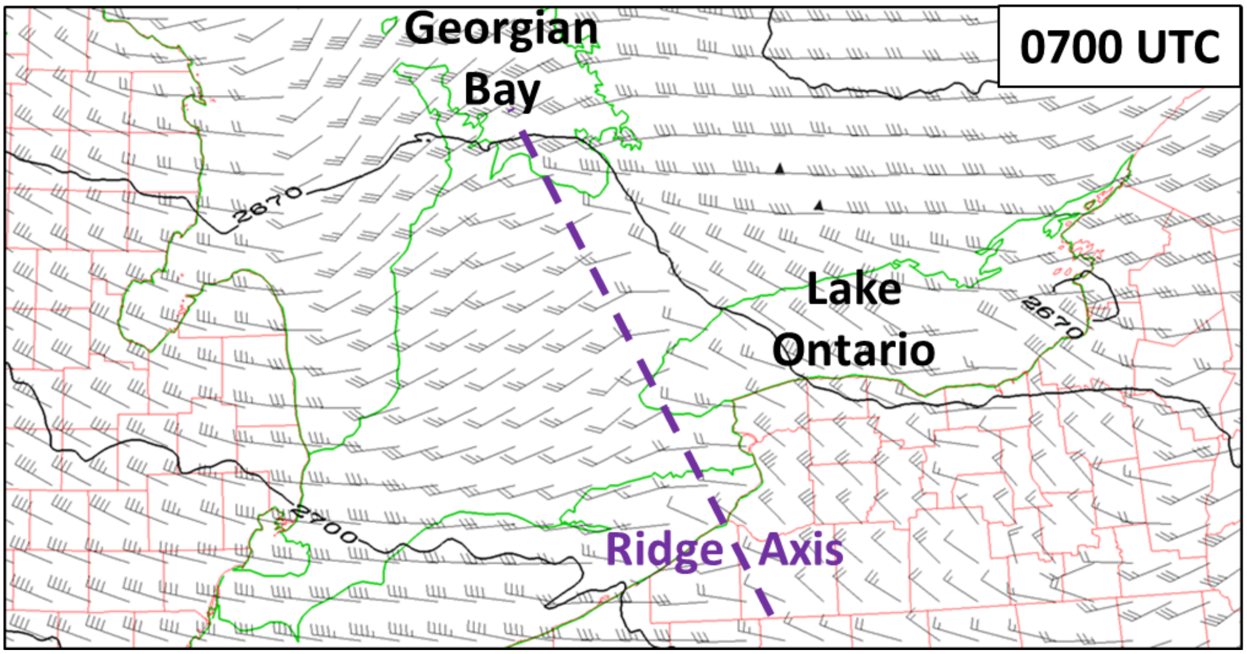

Figure 8. 700-hPa analysis valid at 0700 UTC from a 0300 UTC/07 January 2014 RAP-initialized Weather Research and Forecasting simulation. Geopotential height (m) is in solid black contours and wind barbs (kts) are in black using standard meteorological notation. The location of the ridge axis has been subjectively drawn in the purple dashed line.

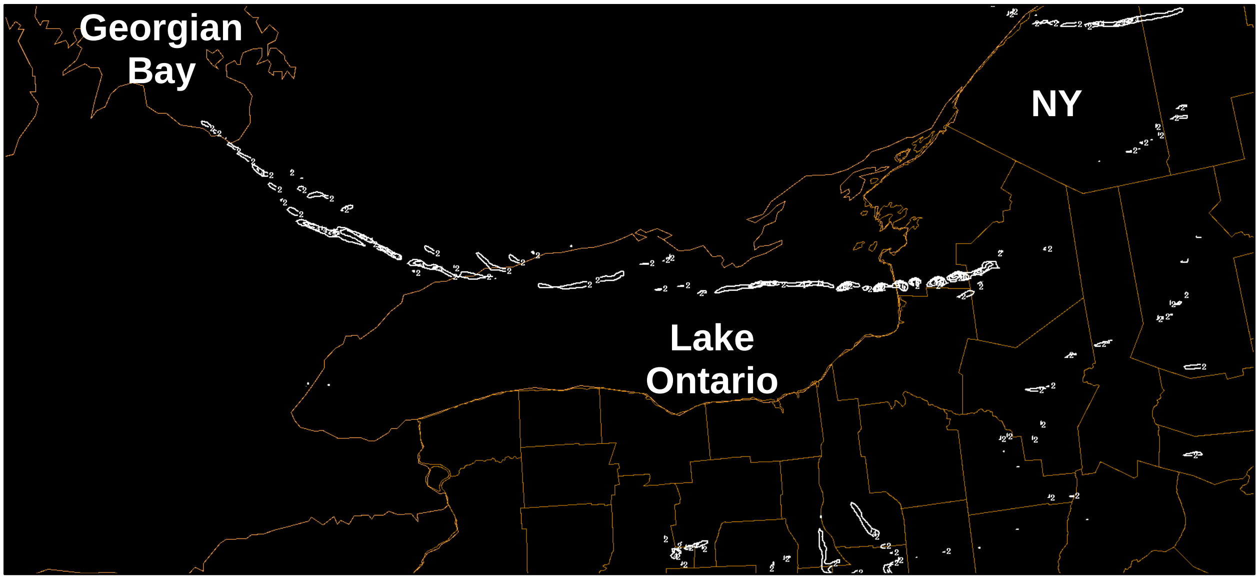

Figure 9. 900-hPa relative vorticity (s^{-1}) valid at 0700 UTC from a 0300 UTC/07 January 2014 RAP-initialized Weather Research and Forecasting simulation.

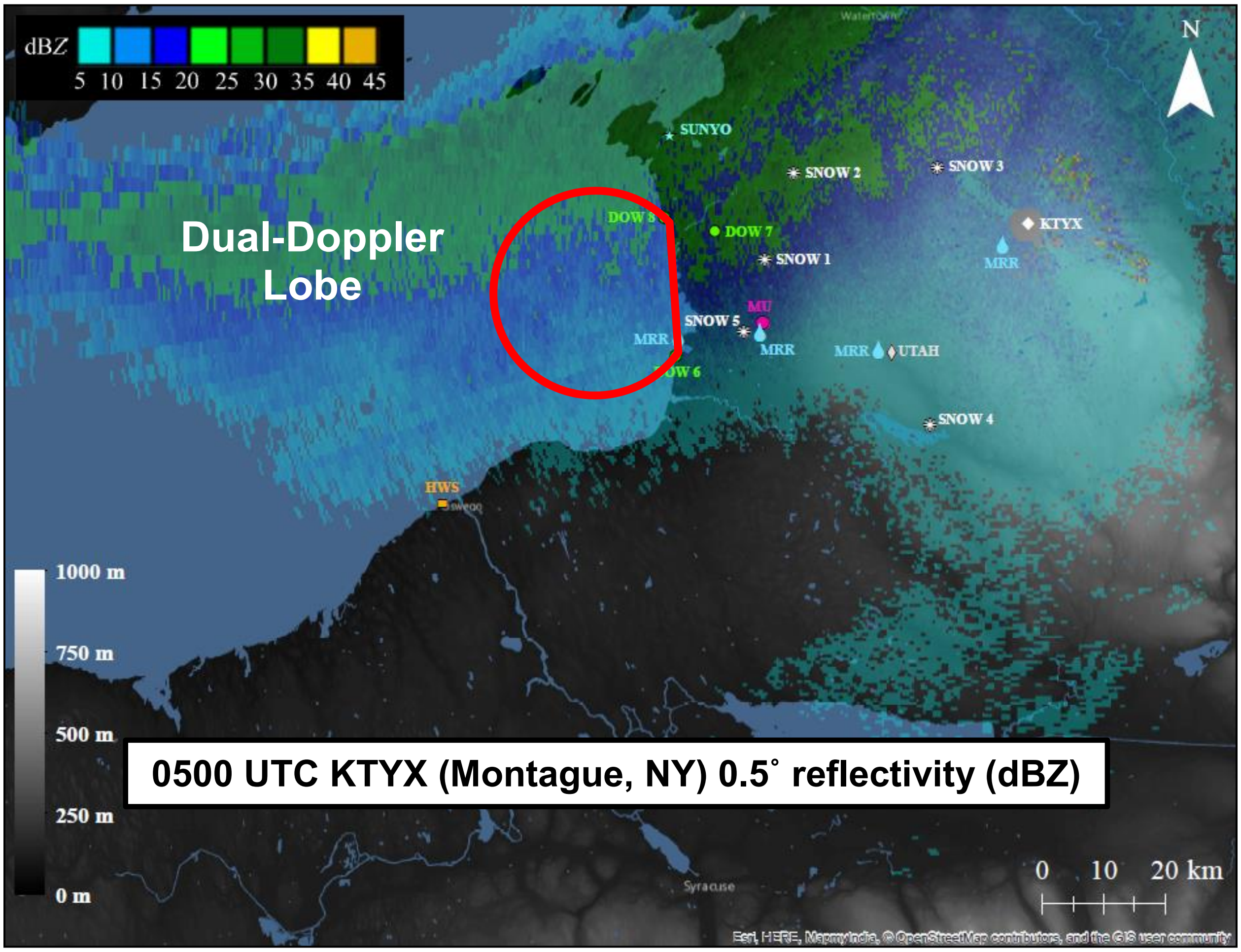

Figure 10. OWLeS asset map from 07 January 2014. The approximate dual-Doppler lobe from DOW6 and DOW8 is drawn in red. The three DOW locations are labeled and marked with green dots, the Montague, NY (KTYX), radar location is labeled and marked with a white diamond, mobile snow-sampling teams are labeled and marked with white asterisks, Microwave Rain Radars (MRR) are labeled and marked with blue rain drops, and the sounding locations are labeled and marked with a variety of colors/symbols (HWS, SUNYO, UTAH, and MU).

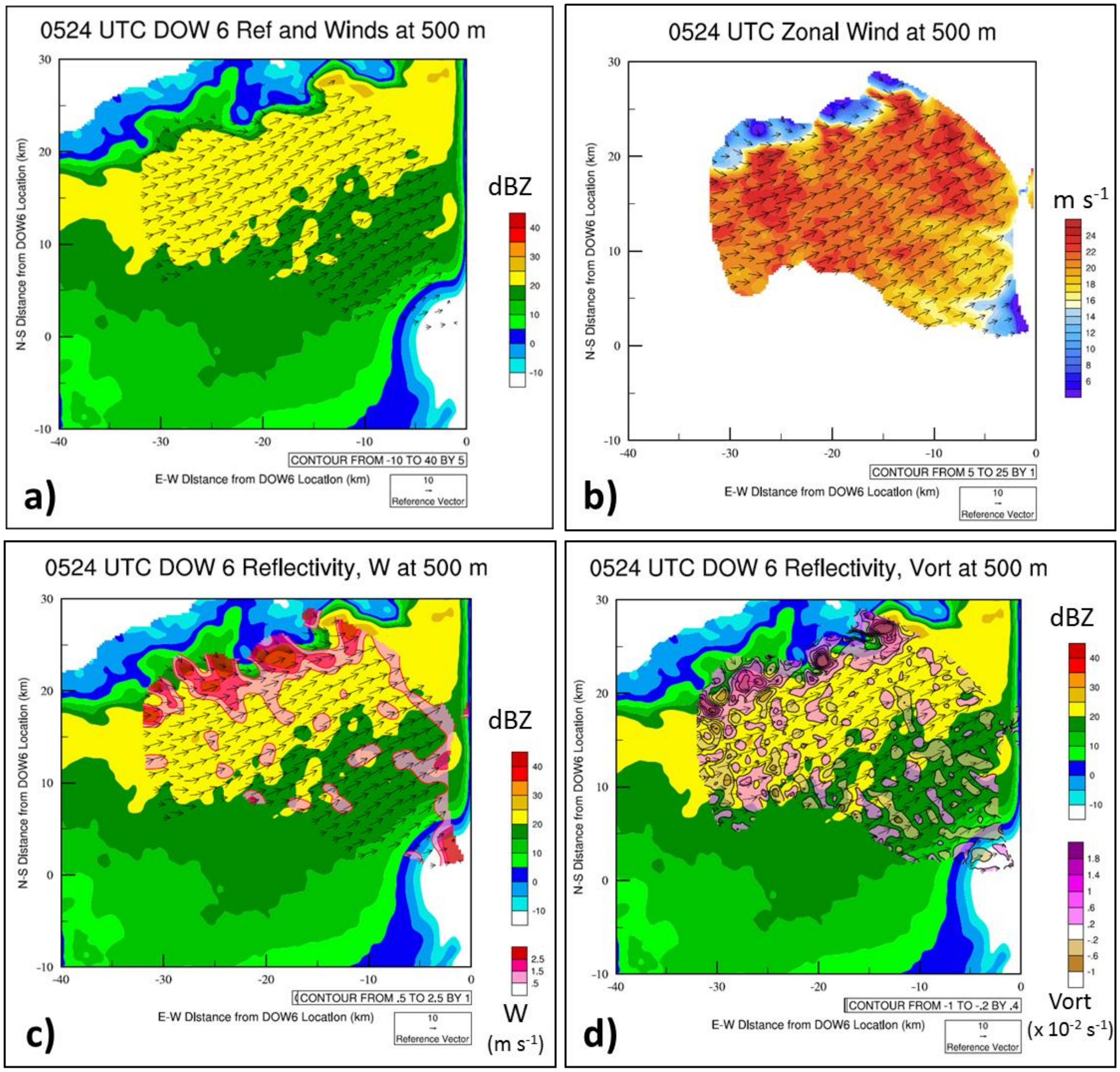

Figure 11a-d. Dual-Doppler wind synthesis at 500 m AGL at 0524 UTC 07 January 2014: a) Reflectivity from DOW6 is plotted every 5 dBZ starting at -10 dBZ and is overlaid with DD-derived winds (black vectors), b) DD-derived winds (black vectors) are plotted along with the zonal wind component (shaded) every 2 m s^{-1}, c) Reflectivity from DOW6 is plotted every 5 dBZ starting at -10 dBZ and is overlaid with DD-derived vertical velocity (red fill colors, only positive values shown) plotted every 1 m s^{-1} starting at 0.5 m s^{-1}, and, d) Reflectivity from DOW6 is plotted every 5 dBZ starting at -10 dBZ and is overlaid with DD-derived relative vertical vorticity (pink and brown fill colors) plotted every 0.4 x 10^{-2} s^{-1}.

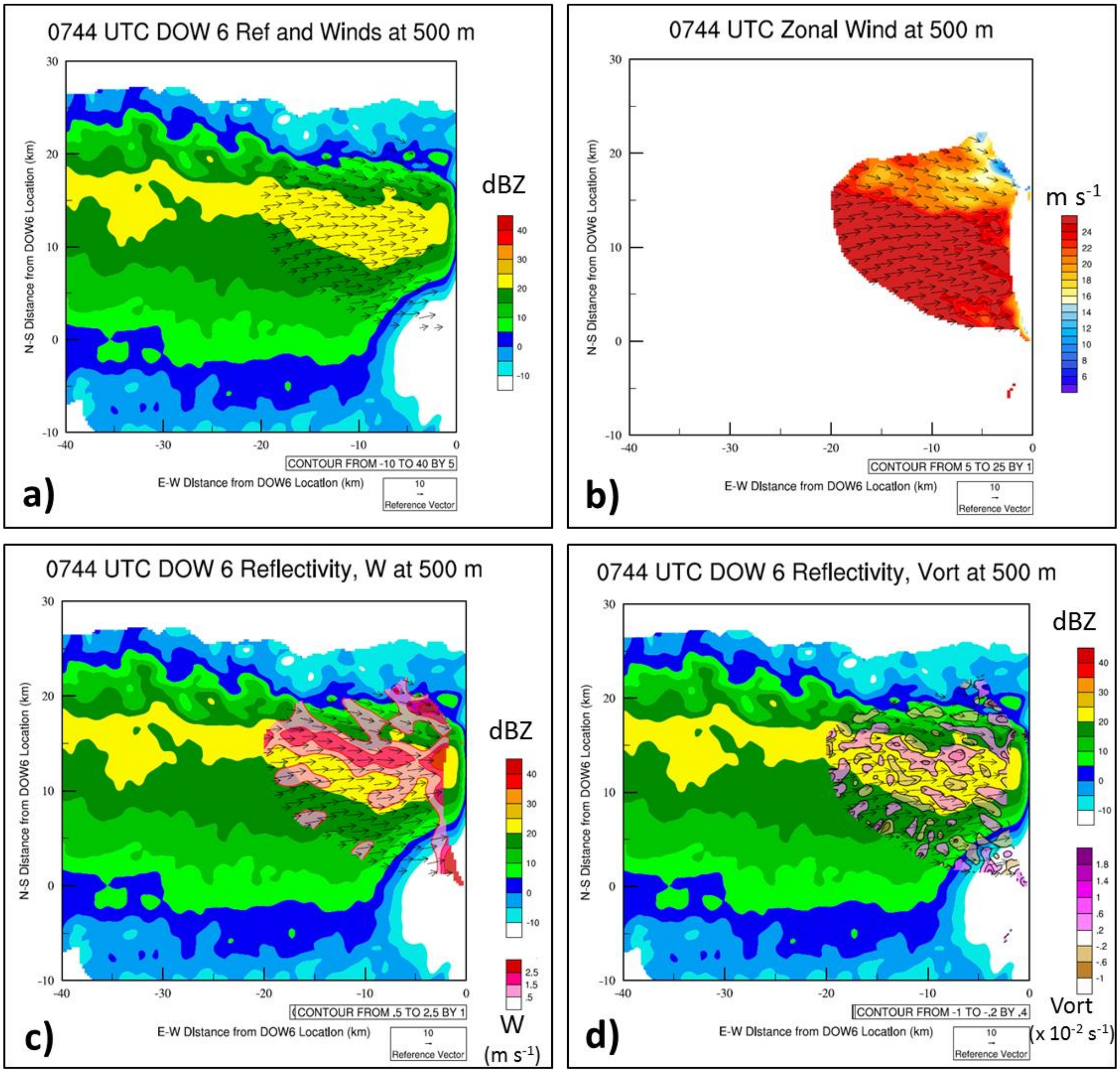

0744 UTC DOW 6 Ref and Winds at 500 m

0744 UTC Zonal Wind at 500 m

0744 UTC DOW 6 Reflectivity, W at 500 m

0744 UTC DOW 6 Reflectivity, Vort at 500 m

Figure 12a-d. As in Fig. 11a-d, but at 0744 UTC.

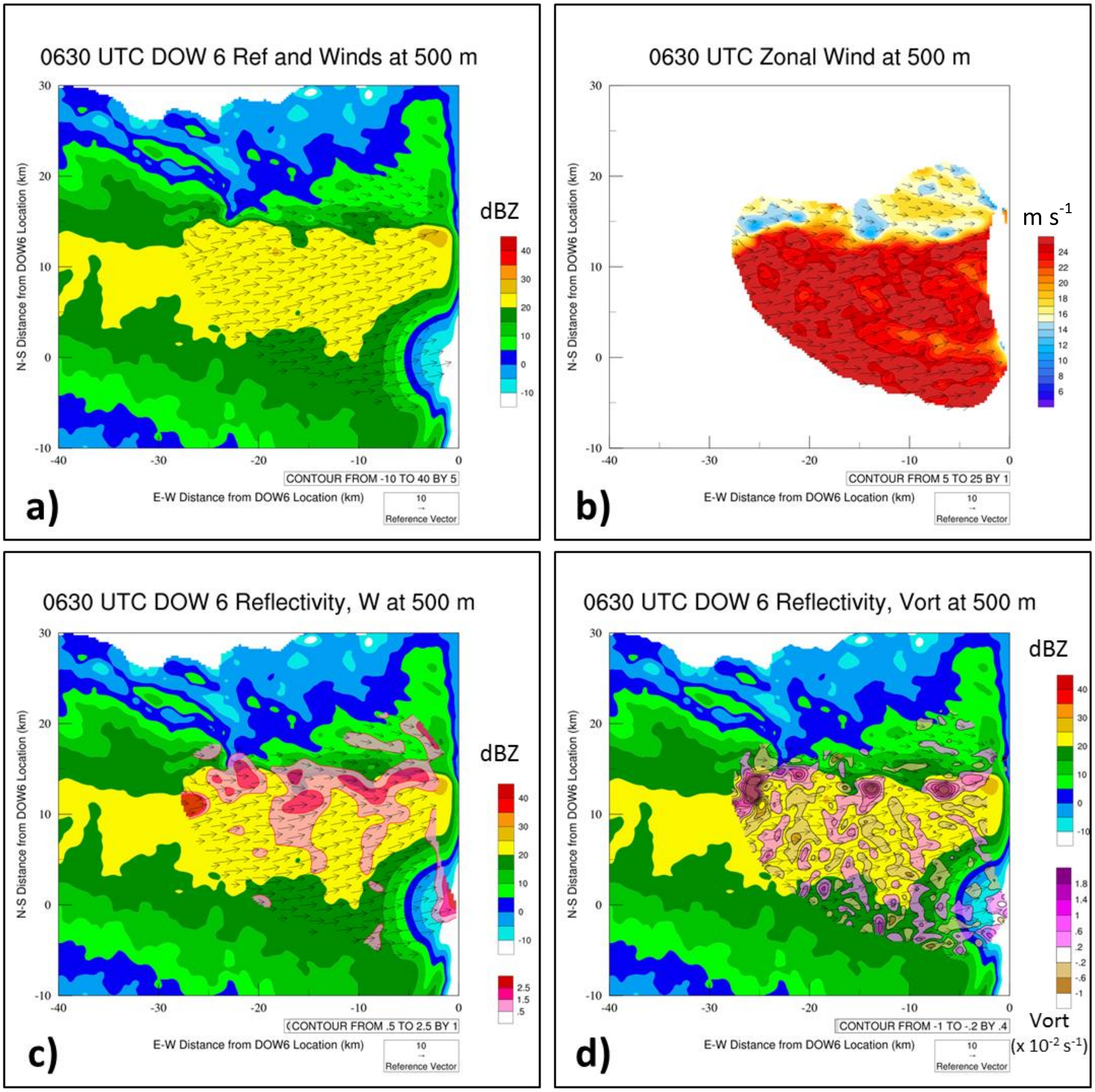

Figure 13a-d. As in Fig. 11a-d, but at 0630 UTC.

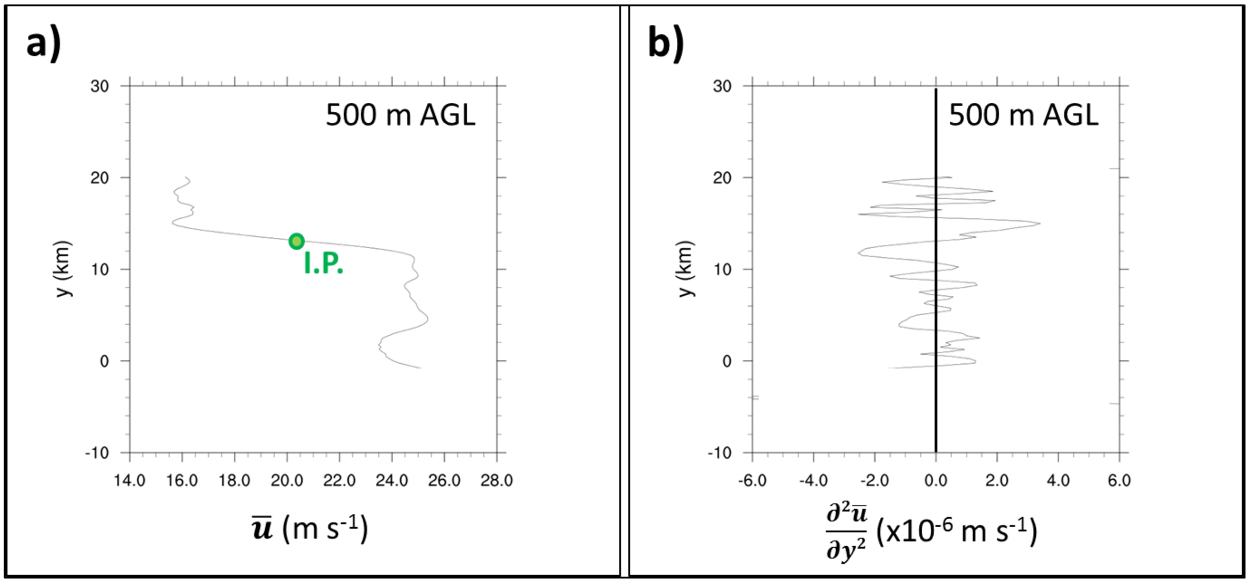

Figure 14a-b. Rayleigh's Stability Criterion at 500 m AGL: a) $\bar{\boldsymbol{u}}$ profile (m s^{-1}), b) $\frac{\partial^2\bar{\boldsymbol{u}}}{\partial^2 \boldsymbol{y}}$ (x10^{-6} m s^{-1}). The green dot denotes the inflection point ("I.P.").

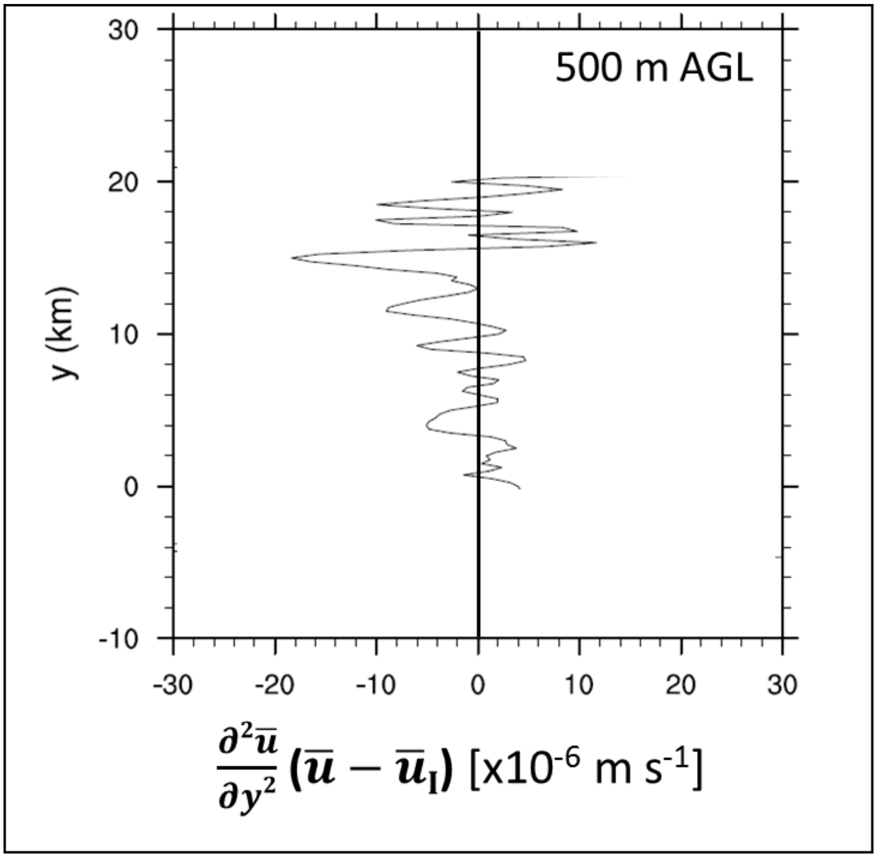

Figure 15. Fjørtoft's Stability Criterion [$\frac{\partial^2\bar{\boldsymbol{u}}}{\partial^2 \boldsymbol{y}}$ $(\bar{\boldsymbol{u}}-\bar{\boldsymbol{u}}_{\boldsymbol{I}})$ (x10^{-6} m s^{-1})] at 500 m AGL.